Highly efficient water desalination through hourglass shaped carbon nanopores

Kurupath, Vishnu Prasad; Kannam, Sridhar Kumar; Hartkamp, Remco; Sathian, Sarith P.

Important note
To cite this publication, please use the final published version (if applicable).
Please check the document version above.

Highly efficient water desalination through hourglass shaped carbon nanopores

Vishnu Prasad Kurupath [a], Sridhar Kumar Kannam [b], Remco Hartkamp [c], Sarith P. Sathian [a,*]

[a] *Department of Applied Mechanics, Indian Institute of Technology Madras, Chennai, India*
[b] *Faculty of Science, Engineering and Technology, Swinburne University of Technology, Melbourne, Victoria 3122, Australia*
[c] *Process and Energy Department, Delft University of Technology, Leeghwaterstraat 39, 2628 CB Delft, the Netherlands*

HIGHLIGHTS

- Water desalination through hourglass shaped carbon nanopores is investigated using molecular dynamics simulations
- Curvature induced density distribution of water inside the nanopores influenced the transport through the nanopores
- The variations in the dipole orientation of water and the hydrogen bonding inside the nanopores correlated with the flow rates
- Insights relevant for the design and fabrication of membranes with nanopores that mimic the shape of biological nanochannels are revealed

ARTICLE INFO

ABSTRACT

Biological nanopores such as aquaporins combine the opposing functions of high water permeation and total ion exclusion in part by the virtue of their hourglass shape. Here, we perform molecular dynamics simulations to examine water and ion conduction through hourglass shaped nanopores created from carbon nanotubes (CNTs) of chirality (6,6), (8,8), and (10,10) in combination with carbon nanocones of half cone angles 41.8°, 30.0°, 19.45°, 9.6° and 0.0°. We observe large variations in flow through the nanopores with change in half cone angles and tube diameters. By computing the pore-water interactions we find a correlated change between the flux and the density profiles of water inside the nanopores. Further, from the orientation, and the hydrogen bonding characteristics of water, we uncover some unexplored facets of flow through hourglass shaped nanopores. The results are insightful for devising novel separation membranes based on nanopores that mimic the shape of biological nanochannels.

1. Introduction

Hydrophobic Carbon Nanotubes (CNTs) hold great potential for applications such as desalination, blue-energy harvesting, drug delivery, lab-on-a-chip, and artificial cells owing to their well-defined diameters that can be leveraged for selective transport, and the nearly frictionless water conduction they exhibit [1–6]. As a result, studies on transport through CNTs having various dimensions [3,7,8], chemical functionalization [9–11], and chirality [12,13] has been conducted, aiming at separation and desalination applications. The flow through CNTs is typically restricted by the hydrodynamic resistance at the pore entrance [14]. Biological nanopores such as aquaporins [15] overcome this limitation by the virtue of their hourglass shape, [16–18] while simultaneously maintaining excellent ion exclusion. As such, these biological

pores display the features of an ideal desalination membrane. Hence, separation membranes with nanopores that mimic the shape of biological nanopores were widely studied [19–21]. However, similar studies on carbon based nanoporous membranes has been minimal.

In an early study, Gravelle et al. [22,23] investigated water permeation through hourglass shaped nanopores using finite-element method and molecular dynamics (MD). Using both analytical and computational methods, they observed an optimum half-cone angle (α), similar in value to the aquaporins, for a given cone-length to pore-radius ratio. Computational studies on aquaporin shaped nanopores created from Lennard-Jones (LJ) particles and layered graphene have been conducted to understand the water conduction and it's mechanism [24–27]. A few studies have specifically focused on hourglass nanopores created from CNTs and carbon nanocones (CNCs). For example, Razmkhah et al. [28]

observed that introducing a conical inlet for CNTs greatly improved the permeability. Li et al. [29,30] investigated the water transport and desalination performance of CNCs with half cone angles (α) 9.6°, 19.45°, 30.0°, and 41.8°. They observed the highest permeation at the angle (α) 9.6° and a maximum ion exclusion when the flow entered the pore at the cone tip, rather than the base. Another study on hourglass nanopores by Zhang et al. [31] revealed that the hydrogen bond reorientation energy plays a major role in entrance effects in CNTs. Further, a recent study on rippled nanocones [32] found that the surface friction and the pore-water affinity imparts large influence on the water conduction. The above studies demonstrate that hourglass shaped nanopores show flow characteristics substantially different from CNTs. For example, a recent study [33] had reported a 3.2 times higher water permeation through hourglass shaped carbon nanopores compared to CNTs of similar diameter. They had attributed this observation to the variation in water dipole orientation inside the hourglass nanopores compared to cylindrical CNTs.

It is thus clear that carbon-based hourglass structures hold great potential as aquaporin mimicking nanoporous membranes [34–36]. Fabrication of such membranes is also technically feasible. Experimentally, CNC arrays of required shapes and angles [37–40], and CNC-CNT composite structures have been successfully achieved [41]. However, there has been minimal studies on water desalination through hourglass shaped carbon nanopores. Further, studies that have observed an optimal conical angle for flow enhancement through similar membranes have not examined the underlying molecular mechanisms in depth. Hence, a detailed investigation is needed to leverage the strength of these nanopores for the optimal design of desalination membranes.

With regard to the aforementioned cause, we have performed molecular dynamics simulations to study desalination through hourglass shaped carbon nanopores by combining CNTs of chirality (6,6), (8,8) and (10,10) and CNCs of half-cone angles (α) 41.8°, 30.0°, 19.45°, 9.6°, and 0.0° ($\alpha = 0.0°$ corresponds to cylindrical CNT). In addition to flow enhancement, we observed an association between the surface curvature and the density structure of water inside the nanopores. Quantifying the dipole variation of water and the hydrogen bond characteristics, we deduce mechanisms responsible for the observed flow characteristics. Our results are essential in understanding flow through hydrophobic hourglass shaped nanopores. Moreover, they reveal multiple critical factors to be considered when designing and fabricating separation membranes based on similar nanopores.

2. Methodology

Fig. 1 shows a representative schematic of the systems used in the study. We used CNTs of chirality (6,6), (8,8) and (10,10) in combination with CNCs of half cone angles (α) 41.8°, 30.0°, 19.45°, 9.6°-which preserved the hexagonal lattice of the CNCs [42]-to create the nanopores. Graphene sheets of dimensions 88 × 88 Å^2 were placed at the reservoir-nanopore junctions and as pistons. Initially, the feed reservoir
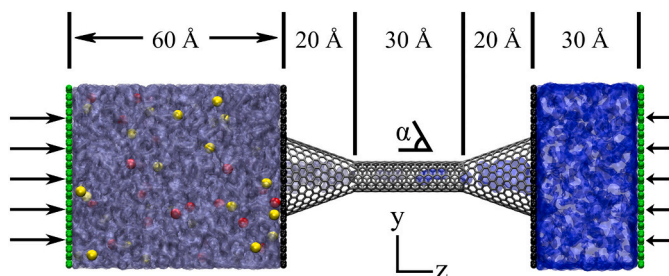
Fig 1. Snapshot of a system used in the study. The blue fluid represents water. The yellow and red spheres represent the sodium and chloride ions. The hourglass shaped wire-mesh at the center represents the nanopore (CNT(6,6), α=19.45°). The green sheets at the ends represent the pistons for pressurizing the reservoirs.

(60 Å long) was filled with 14,550 water molecules, and 139 Na$^+$ and Cl$^-$ ions, corresponding to a 0.5 M solution. This concentration is approximately representative of seawater. The permeate reservoir (30 Å long) contained 7311 water molecules. The nanopore contained 41 to 233 water molecules depending on the pore size. A vacuum slab of length 60 Å was added beyond both the piston sheets to avoid interactions between the pistons across the periodic boundary (along z-axis).

The SPC/E model [43], which can reproduce the bulk transport coefficients of water [44] and slip lengths through hydrophobic surfaces with good accuracy [45] was used to represent the water. The ion and carbon interactions were modelled using the parameters from Cohen-Tanugi and Grossman [46]. The remaining cross interaction parameters were determined using Lorentz-Berthlot mixing rule (see Table S1 in Supplementary Info (SI)). A cut off of 12 Å was used for the LJ and Coulombic interactions. Long range electrostatic forces were corrected using the Particle-Particle Particle-Mesh (PPPM) method [47]. The SHAKE algorithm [48] was used to keep the bonds and angles of water molecules rigid. Periodic boundary conditions were applied in all directions and a timestep of 1 fs was used. The simulations were carried out using the LAMMPS package [49].

After an initial energy minimization, the system was equilibrated for 5 ns at 300 K using a Nosé-Hoover thermostat applied to the fluid. During the equilibration, opposing constant external forces of equal magnitude were applied to both the pistons along the z-axis to generate a pressure of 1 atm in the reservoirs. During the production run, the force on the feed side piston was increased to generate 200 MPa pressure, while the permeate side pressure was maintained at 1 atm. Such an excessively large pressure gradient was necessary to generate statistically significant results from a limited simulation time due to the fact that the thermal motion of molecules in nanoscale flows are large compared to the streaming motion. The production run was carried out for 4 ns and 5 independent simulations were conducted for each geometry considered in this study to obtain statistically consistent results from a small simulation time. The number of water molecules crossing the nanopore was sampled every 100 fs and the trajectories were recorded every 200 fs for further analysis.

The hydrogen bonds were defined using a geometric criterion where two molecules were considered hydrogen bonded if the donor and acceptor oxygen were within 3.5 Å and the angle between the donor-hydrogen-acceptor was greater than 140° [50]. The components of the unit dipole vector in cylindrical coordinates were calculated by first calculating the absolute axial and radial components ($|\hat{p}_z|$ and $|\hat{p}_r|$) of the unit dipole vector. The theta component of the unit dipole vector ($|\hat{p}_\theta|$) was defined as the component perpendicular to both the radial and axial directions of the nanopore, tangential in direction to the nanopore curvature. $|\hat{p}_\theta|$ was estimated using the following equation (see SI for more details):

$$|\hat{p}_\theta| = \sqrt{|\hat{p}|^2 - \left(\left|\hat{p}_z\right|^2 + \left|\hat{p}_r\right|^2\right)} \qquad (1)$$

3. Results and discussion

Fig. 2(a) shows the number of water molecules (N_w) crossing the CNT (8,8) nanopores at different half cone angles (α) against time (t). Similar plots for CNT(6,6) and the CNT(10,10) nanopores are given in Fig. S1 of the SI. The number of water molecules varied linearly against the time with the slope indicating the flux (Q_w). Among the nanopores, the maximum flux was observed at the half cone angle 9.6° while the minimum flux was observed at 0.0° (cylindrical CNT), confirming to previous results [29,30]. Fig. 2(b) shows the water and ion flux (Q_w and Q_i) through the nanopores against the half cone angle. The flux showed a direct dependence on both the CNT size and the half cone angle. Except for the CNT(6,6) nanopores, the ion and the water flux trends obtained were close to each other. In CNT(6,6) nanopores there was zero ion
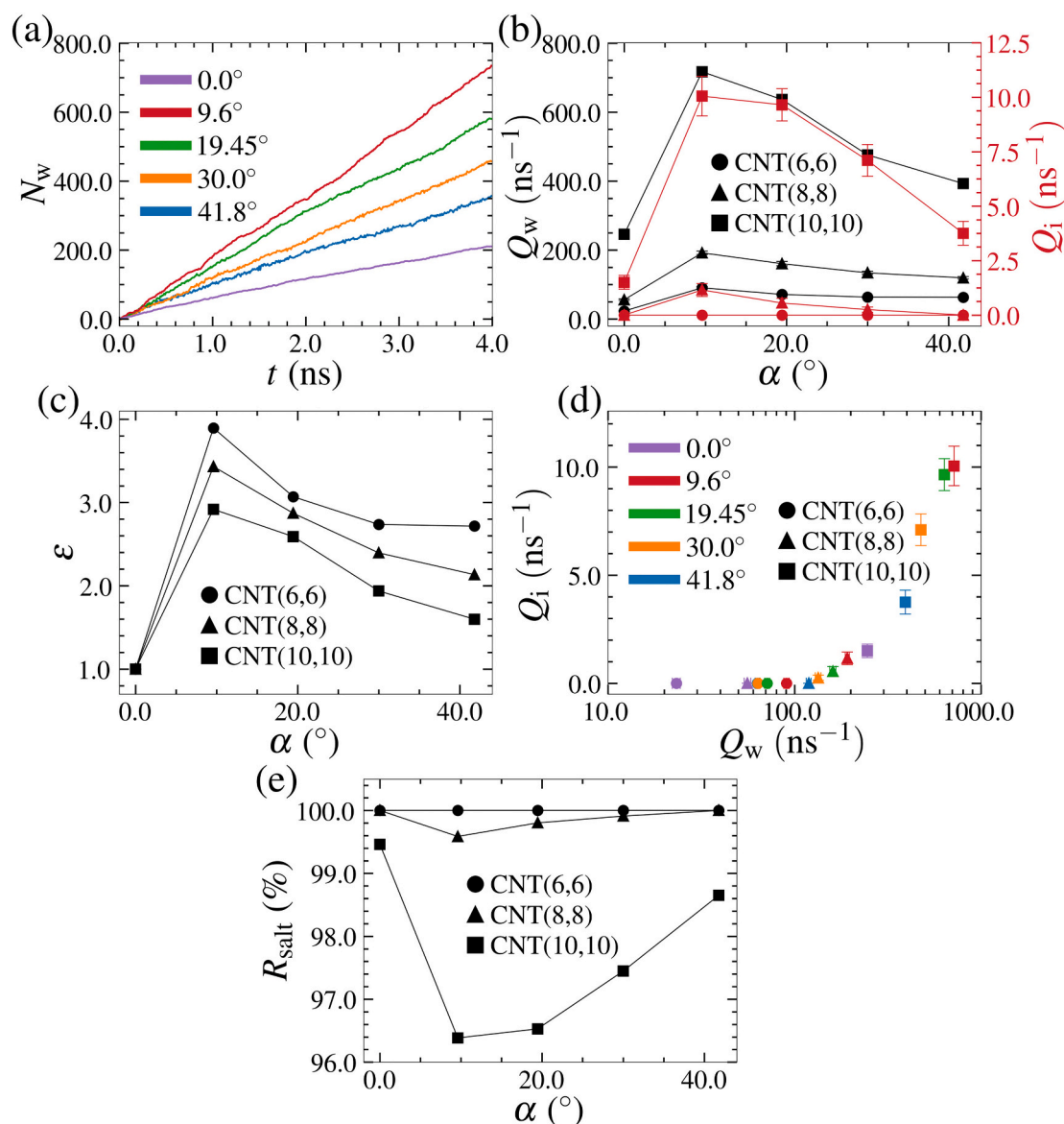
Fig. 2. (a) The number of water molecules (N_w) crossing the CNT(8,8) nanopores against time (t). (b) The water flux (Q_w) and the ion flux (Q_i) through the nanopores against the half cone angle (α). (c) Flow enhancement (ε) through the nanopores against the half cone angle. (d) Ion flux (Q_i) against the water flux (Q_w) through the nanopores. The marker colors represent the half cone angle and the marker shapes represent the CNT chirality. (e) The salt rejection (R_{salt}) achieved by the nanopores against the half cone angle.

conduction irrespective of the half cone angle due to the strong size exclusion of ions inside the tubes [3]. Fig. 2(c) shows the flow enhancement (ε)-calculated as the flux through the nanopores normalized by the flux at $\alpha = 0.0°$ (cylindrical CNT)-against the half cone angles. Contrary to the flux values (Fig. 2(b)), the maximum enhancement was observed in the CNT(6,6) nanopores, while the minimum enhancement was shown by the CNT(10,10) nanopores. This indicates that the effect of conical entrance on water conduction is higher when the nanopore diameter is small. Further, the enhancement varied minimally between the nanopores with high half cone angles, i.e., between angles 41.8° and 30.0°. These results are a consequence of the curvature effects and the structuring of water inside the nanopores which are discussed in Figs. 3 and 4. Fig. 2(d) shows the ion flux (Q_i) against the water flux (Q_w) through the nanopores. The marker colors are used to represent the half cone angle and the marker shapes represent the CNT chirality. The ion permeation was found to be closely associated with the water permeation through the nanopores. Water flux through CNT(8,8)-41.8° nanopore is the threshold value of water permeation that the nanopores could achieve without ion

leakage indicating the permeability-selectivity threshold. With a reduction in the half cone angle in CNT(8,8) from 41.8°, the water flux increases through the nanopore and ion permeation also ensues. Since ion permeation through CNTs directly depend upon the applied pressure [8], the ion exclusion reported here are conservative estimates. The cylindrical CNT(8,8) ($\alpha = 0.0°$) showed zero ion conduction for our SPC/E water solution contrary to the results obtained using the TIP3P model [3,51]. This is a consequence of the lower and more accurate diffusion coefficient and the consequent lower flux shown by the SPC/E water through the nanopores compared to the TIP3P model [44,52,53]. The salt rejection (R_{salt}) achieved by the nanopores is provided in Fig. 2(e) (see SI for details). The salt rejection followed a trend opposite to that of the ion permeation shown in Fig. 2(b). The CNT(6,6) nanopores showed total salt rejection, while in wider CNTs, the salt rejection was reduced. The salt rejection in CNT(8,8) and CNT(10,10) nanopores were the highest for cylindrical CNTs ($\alpha = 0.0°$). With the introduction of conical entrances, the salt rejection in CNT(8,8) and CNT(10,10) nanopores reduced with reduction in the half cone angle. The trends obtained for the salt rejection
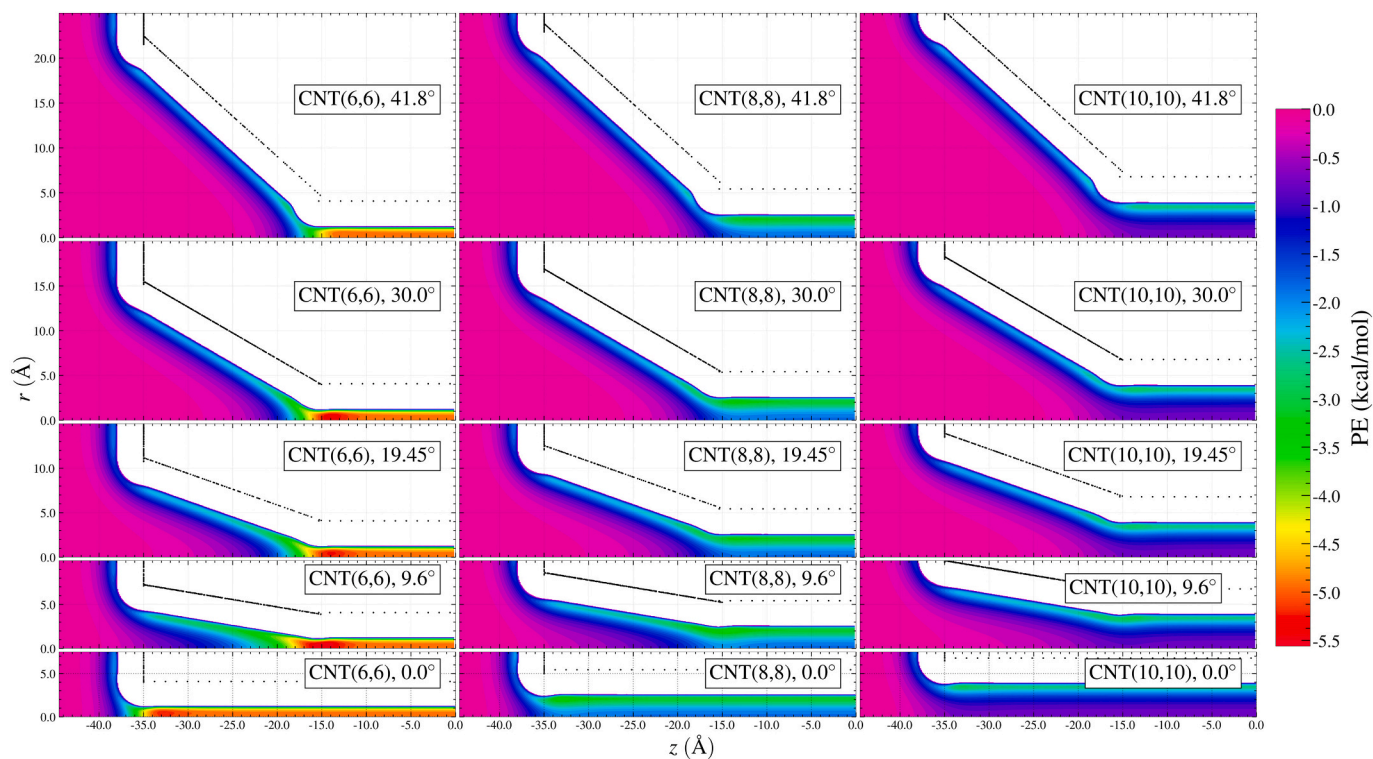
Fig. 3. Potential energy (PE) of an isolated water molecule inside the nanopore. Cylindrical coordinates (r and z) are used for the plot (r and z). The black dots represent the carbon atoms of the nanopore. PE values above zero and values in sample space outside the nanopore are neglected for clarity. The height to width ratios of the nanopores are preserved in the plots so that the entrance angles are not skewed.
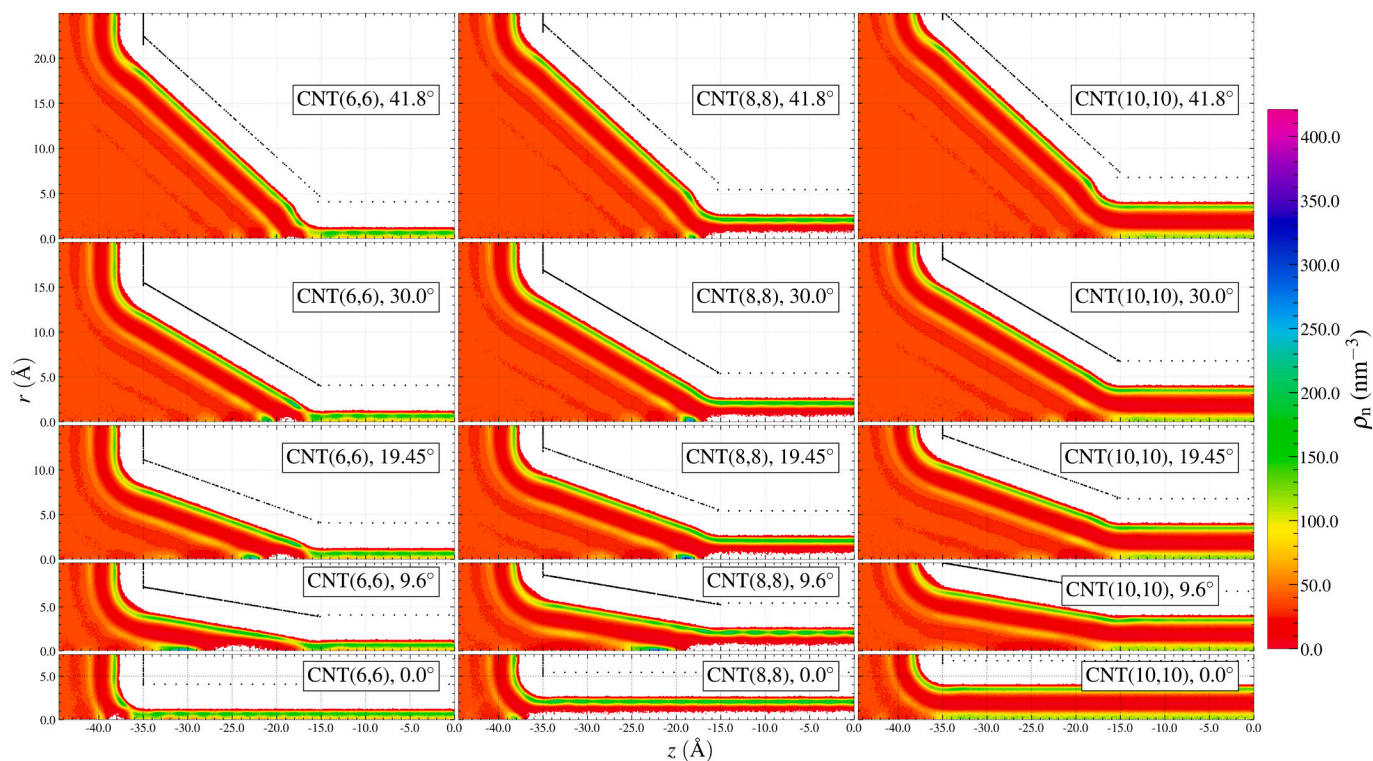
Fig. 4. The number density of water (ρ_n) inside the nanopores. Cylindrical coordinates are used for the plot. The black dots represent the carbon atoms of the nanopore. Coordinate space unsampled by water are excluded from the plot. The height to width ratios of the nanopores are preserved in the plots so that the entrance angles are not skewed.

Table 1
The water flux (Q_w, ns^{-1}), the ion flux (Q_i, ns^{-1}), the flow enhancement (ε) and the salt rejection (R_{salt}, %) through the nanopores at different CNT chirality and half cone angles (α, °).

CNT	α	Q_w	Q_i	ε	R_{salt}
	41.80	63.15	0.00	2.72	100.0
	30.00	63.60	0.00	2.74	100.0
(6,6)	19.45	71.35	0.00	3.07	100.0
	9.60	90.55	0.00	3.89	100.0
	0.00	23.25	0.00	1.00	100.0
	41.80	119.25	0.00	2.13	100.0
	30.00	133.85	0.25	2.39	99.91
(8,8)	19.45	160.45	0.55	2.87	99.80
	9.60	191.85	1.15	3.43	99.59
	0.00	55.90	0.00	1.00	100.0
	41.80	392.65	3.75	1.60	98.65
	30.00	475.90	7.10	1.94	97.45
(10,10)	19.45	636.40	9.65	2.59	96.53
	9.60	716.95	10.05	2.92	96.38
	0.00	245.70	1.50	1.00	99.46

in CNT(8,8) and CNT(10,10) nanopores follow the close correlation observed between the water and ion transport observed across the nanopores (Fig. 2(d)). Table 1 shows the data corresponding to Fig. 2.

For all the CNTs studied, the optimum half cone angle obtained was 9.6°. This is in line with the theoretical predictions by Gravelle et al. [22]. Assuming that the half cone angle can take a continuous value, and using the analytical formula for hydrodynamic resistance obtained by Gravelle et al. [22], we find that the optimum half cone angles for nanotubes with radii equal to CNT(6,6), CNT(8,8) and CNT(10,10) are 11.40°, 13.20°, and 14.70° (see Eq. (1), and Fig. S2 in SI). We quantified the normalized hydrodynamic resistance obtained from the analytical solution at the half cone angles 9.6° and 19.45° (see Table S2 in the SI). Except in CNT (10,10), the normalized hydrodynamic resistance was minimum at $\alpha = 9.6°$. In CNT(10,10), the normalized hydrodynamic resistance at $\alpha = 19.45°$ is higher than at $\alpha = 9.6°$. This is in contradiction to the flow rates and the optimal half cone angle observed in Fig. 2. However, the analytical solution reported by Gravelle et al. [22] have assumed a frictionless flow through the CNC section of the nanopore. If the contribution of friction is also taken into account, there would be a higher frictional resistance to flow at the CNC section when the half cone angle is 19.45° compared to 9.6°. This is a consequence of the increase in the surface area of the CNC. Further, the viscosity variation inside the nanopores is not considered. Hence the observed flux values, and the optimal half cone angle obtained for the nanopores are justified.

Fig. 3 shows the potential energy (PE) of an isolated water molecule inside the nanopore with the center of oxygen assumed as the molecule center. Cylindrical coordinates were used in the plots (see SI for details). In cylindrical CNTs ($\alpha = 0.0°$), the depth of PE reduced as the CNT size increased due to the weaker curvature effects present inside the wider CNTs [54,55]. The potential energy changed steeply at the cylindrical CNT entrances ($z = -35.0$ Å) and at the CNC-CNT junction ($z = -15.0$ Å) of nanopores with large half cone angles ($\alpha = 41.8°$, 30.0° and 19.45°). However, the change in PE inside the nanopores with lower conical angles ($\alpha = 9.6°$) were gradual, especially when the CNT diameter was small. For example, the PE change along the axis of the CNT(6,6)-9.6° nanopore spans from $z = -30.0$ Å to $z = -15.0$ Å. Whereas PE change along the CNT(8,8)-9.6° nanopore axis spans from -25.0 Å to -15.0 Å (see Fig. S3 in SI). However, this effect was minimal in the CNT(10,10) nanopores due to their increased size.

Fig. 4 shows the number density of water (ρ_n) inside the nanopores in cylindrical coordinates (r and z). The density profiles showed layering at the inner surfaces of the nanopores [55–57] arising from the strong interaction potential present near these surfaces (see Fig. 3). Similar to PE, the density layering structure inside the CNCs remained identical between the nanopores at large half-cone angles (41.8°, 30.0° and 19.45°). Furthermore, the density structure changed drastically at the

cylindrical CNT entrances ($z = -35.0$ Å), and at the CNC-CNT junctions ($z = -15.0$ Å) due to curvature effects when moving into the CNT. However, at smaller half cone angles ($\alpha = 9.6°$), the density structure of water inside the CNCs deviated from the regular layered structure and the transformation towards the CNT interior was more gradual. This effect became less evident with increase in the CNT size, consistent with the PE profiles. Hence, the density structure observed inside the nanopores can be assumed as a consequence of the PE profile of isolated water inside the nanopores. This is further evident from the close reciprocity that is seen between the density and the PE along the nanopore axis (see Fig. S3 in SI). Further, the PE and the consequent density structuring explains the flow enhancement values observed through the nanopores (Fig. 2 (c)). When the CNT is narrow, there is a strong influence of PE inside the tube and correspondingly on the density structuring. Introduction of conical inlet to such CNTs creates increased density alterations at the entrance of the nanopores, leading to a high flow enhancement. When the CNT is wide, the strength of the curvature-induced PE and the density structuring is less significant and consequently, the enhancement in those nanopores are reduced. The density profiles obtained inside the cylindrical CNTs were in agreement with previous studies [58–61].

To understand the flow mechanism through the nanopore, we calculated the probability density of water, only considering the contribution from the water molecules that crossed the nanopore, shown in Fig. 5 (see SI for details). The probability density of water was found to be high at the inner surface of the CNCs and CNTs, and very minimal near the axis. This indicates that most water molecules that crossed the nanopore moved preferably adjacent to the inner surfaces of the nanopores, away from the pore axis. This is also unambiguous since the cylindrical binning implicitly creates bins of larger volumes at locations away from the axis (see Fig. S3 in SI). Inside the cylindrical CNTs ($\alpha = 0.0°$), the probability density was higher than in hourglass nanopores due to their lower flow rates. Whereas, the probability density within the hourglass nanopores was high at the CNC section and much leaner at the CNT section. This is due to the relative accumulation of water molecules inside the CNC section of the nanopore compared to the CNT portion, as explained below.

Fig. 6 shows the percentage time (t_p) taken by the water molecules to cross the nanopore, spanning from $z = -45.0$ Å to $z = 0.0$ Å (similar graphs for water molecules crossing from $z = -35.0$ Å to $z = 35.0$ Å are provided in Fig. S5 of the SI). In all the cases t_p showed an increase in slope against z before the reservoir-CNC junction indicating blockage before entering the nanopores. Inside the cylindrical CNTs ($\alpha = 0.0°$), the curves showed a linear trend, implying that the molecules spends relatively equal amount of time at all the locations along its path. In hourglass nanopores ($\alpha \neq 0.0°$), the slope was small ahead of the reservoir-CNC junction indicating a relatively fast flow. However, the slope got steep inside the CNC indicating a relative stagnation inside the CNC. This stagnation arises from the crowding of water molecules inside the CNC section as the cross sectional area decreases. The slope decreased before the CNC-CNT junction indicating a relatively fast entry into the CNT. With an increase in CNT size, the offset to the decrease in the slope before the CNC-CNT junction were larger, indicating a lower stagnation inside the CNCs. Additionally, the overall slope inside the CNC section also reduced with an increase in the CNT size. At $\alpha = 9.6°$ the curves showed a slope that is smaller than the other hourglass nanopores. Also, the offset to the the decrease in slope before the CNC-CNT was larger when α was 9.6° compared to the other half cone angles. This implies that, when $\alpha = 9.6°$, the t_p against z curve slopes vary less before both the reservoir-CNC and the CNC-CNT junctions. Hence, when $\alpha = 9.6°$, (1) the relative stagnation of molecules before the reservoir-CNC junction and inside the CNC are similar, and (2) there is relatively less stagnation inside the CNC compared to other nanopores.

Fig. 7 shows the components of the unit dipole vector ($|\hat{p}_r|$, $|\hat{p}_z|$ and $|\hat{p}_\theta|$) of the water molecules against z (see methodology and the SI for
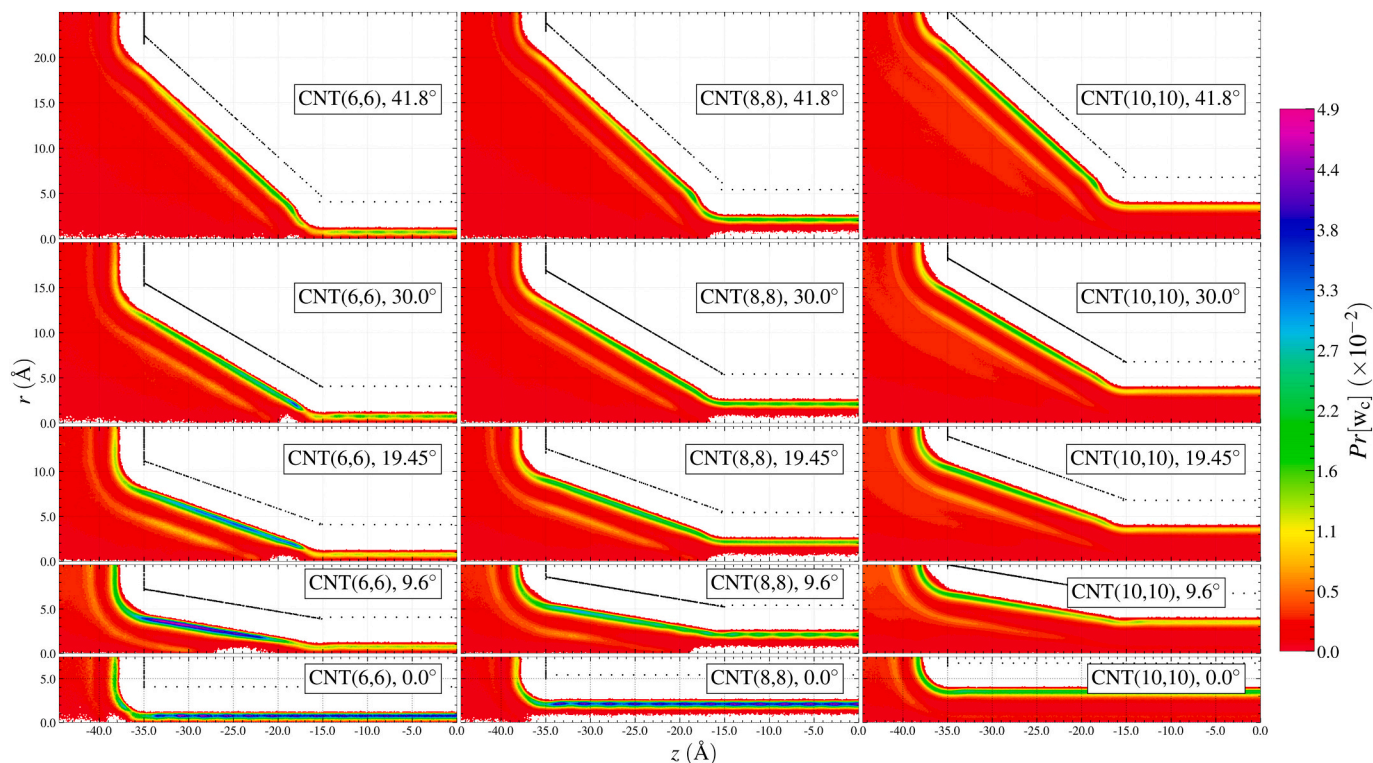
Fig. 5. Probability density of water that crossed the nanopore ($Pr[w_c]$). Cylindrical coordinates are used for the plot. The black dots represent the carbon atoms of the nanopore. Coordinate space unsampled by water are excluded from the plot. The height to width ratios of the nanopores are preserved in the plots so that the entrance angles are not skewed.
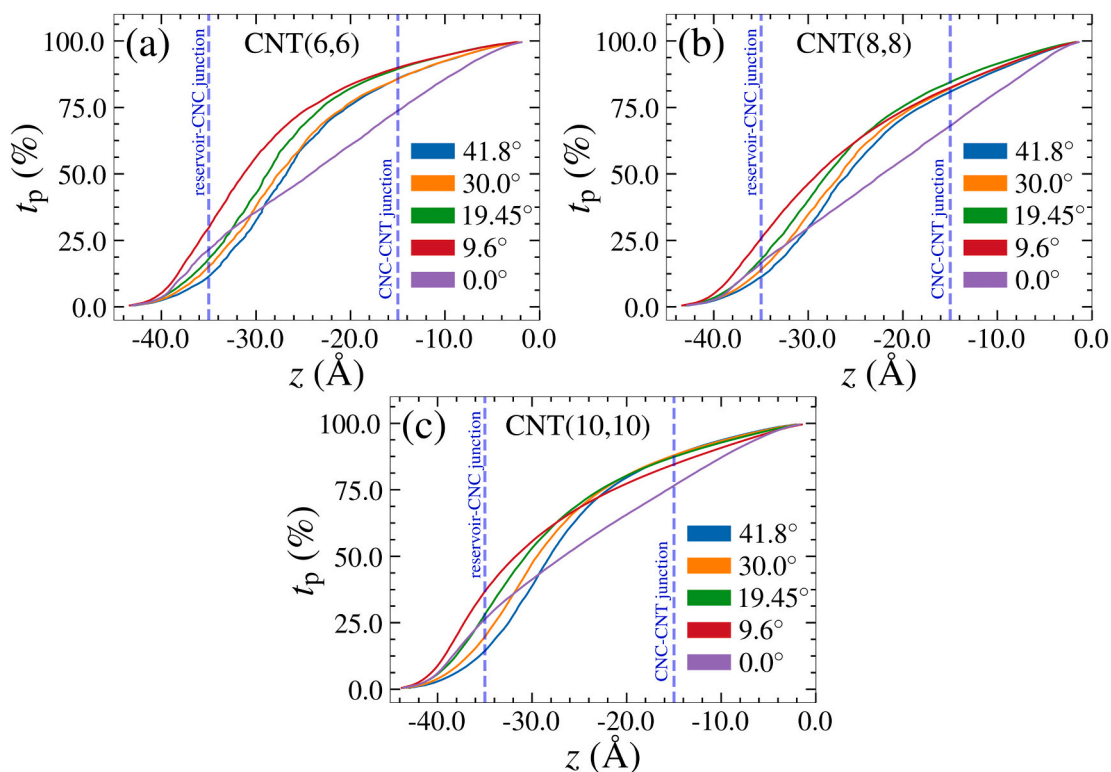
Fig. 6. The percentage time (t_p) taken by the water molecules to cross the nanopore along z (from $z = -45.0$ Å to $z = 0.0$ Å). Plots (a), (b) and (c) represent the results for CNT(6,6), CNT(8,8) and CNT(10,10) nanopores. The blue vertical lines indicate the reservoir-CNC junction ($z = -35.0$ Å) and the CNC-CNT junction ($z = -15.0$ Å).
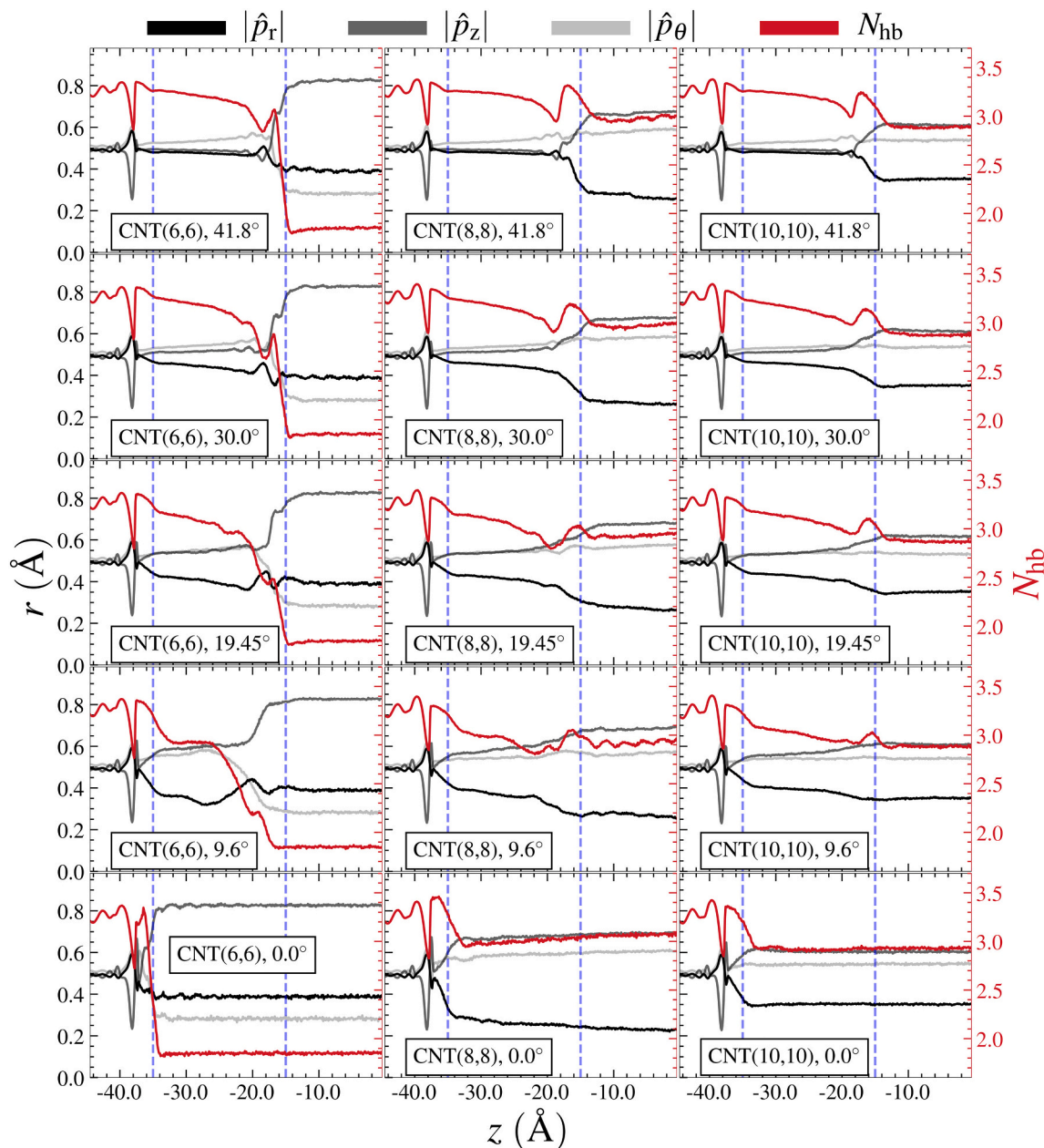
Fig. 7. The r, z and the θ components of the unit dipole of water ($\hat{p}$) along the pore length (left axis, lines in shades of black). The number of hydrogen bonds (N_{hb}) along the pore length (right axis, red line). The blue vertical lines indicate the reservoir-CNC junction ($z = -35.0$ Å) and the CNC-CNT junction ($z = -15.0$ Å).

calculation details). The number of hydrogen bonds (N_{hb}) are also given on the right axis (red lines). The hydrogen bond count in the bulk is in agreement with previous studies [52,62]. The dipole orientation and the number of hydrogen bonds varied simultaneously at specific points inside the nanopores. In cylindrical CNTs ($\alpha = 0.0°$), both the dipole orientations and the hydrogen bond count varied significantly at the CNT entrance ($z = -35.0$ Å) and remained constant inside the CNTs. In hourglass nanopores ($\alpha \neq 0.0°$), the orientations and the hydrogen bond count varied gradually inside the CNCs. As the half cone angle increased, the orientations varied to a higher extend at the reservoir-CNC junction and to a lower extend at the CNT-CNC junction. As the half cone angle decreased, the orientations varied to similar extends at both the reservoir-CNC and the CNT-CNC junctions. This trend was very apparent in the CNT(6,6) nanopores for the cases of the orientations and the hydrogen bond count. However, the hydrogen bond count between the reservoir and the wider CNTs (CNT(8,8) and CNT(10,10)) differed only to a small extend. Hence, there was very little difference between the

hydrogen bond count profiles across different half cone angles in the those nanopores. Meanwhile, the dipole orientations inside the CNT (8,8) and CNT(10,10) nanopores showed variations of similar extend at the reservoir-CNT and CNT-CNC junctions at lower half cone angles, similar to the CNT(6,6) nanopores.

The dipole orientation and the hydrogen bond count profiles are indicative of the energy changes that water molecules undergo when moving through the nanopore. Previously, the activation energy associated with the movement of water molecules has been directly related to the flow viscosity [63]. Hence, we deduce that the fluid viscosity inside the nanopores changes in close relation with the hydrogen bonding and the orientations. This implies that when the half cone angle increases, the fluid viscosity change occurs primarily at the CNC-CNT junction. Similarly, when the half cone angle reduces, the viscosity change is distributed between the reservoir-CNC junction and the CNC-CNT junction. A similar observation has also been made by Gravelle et al. [22], where, at the optimum half cone angle (α_{opt}), the viscous

dissipation at the reservoir-CNC junction and the CNC-CNT junction were found to have intermediate values such that the net viscous dissipation through the nanopore was minimized. Hence, the difference in distributions of fluid viscosity between the reservoir-CNC and the CNC-CNT junction arising from the dipole orientations and the hydrogen bonding leads to the flow enhancements observed through the nanopores.

4. Conclusions

We have presented a molecular dynamics simulation study of water transport and desalination across hourglass shaped nanopores created using CNT(6,6), CNT(8,8), and CNT(10,10) combined with CNCs of half cone angles 41.8°, 30.0°, 19.45°, 9.6°, and 0.0°. We have found that the flux through the nanopores was highest for a half cone angle of 9.6°. Further, we observed that narrow CNTs yielded a larger flow enhancement than wider CNTs. That was attributed to change in curvature-induced interactions and the resulting density structure of water. We also deduced that the differences in dipole orientation and the hydrogen bonding inside the nanopores induce diverse viscosity distributions between the reservoir-CNC junction and the CNC-CNT junction. This in turn translates into the flow enhancements shown by the nanopores.

Our results show that the flow through hourglass shaped carbon nanopores are highly influenced by the half cone angle at the pore entrance and the local structure of water inside the nanopores determine the enhancement obtained. Our results explain some determining factors of water transport through nanopores with shapes resembling biological nanochannels such as aquaporins. The results also provide insights for devising separation membranes based on hourglass shaped nanopores. Further, novel nanopore shapes can be conceived from the understanding derived on how the structure of water and the pore shape are related.

CRediT authorship contribution statement

Vishnu Prasad K: Conceptualization, Methodology, Software, Investigation, Formal Analysis, Visualization, Writing-Original Draft.
Sridhar Kumar Kannam: Conceptualization, Software, Writing-Review and Editing.
Remco Hartkamp: Visualization, Validation, Writing-Review and Editing.
Sarith P Sathian: Methodology, Investigation, Formal Analysis, Validation, Writing-Review and Editing, Supervision.

Declaration of competing interest

The authors declare that they have no known competing financial interests or personal relationships that could have appeared to influence the work reported in this paper.

Appendix A. Supplementary data

Supplementary data to this article can be found online at https://doi.org/10.1016/j.desal.2021.114978.

References

[1] G. Hummer, J.C. Rasaiah, J.P. Noworyta, Nature 414 (2001) 188.
[2] E. Secchi, S. Marbach, A. Niguès, D. Stein, A. Siria, L. Bocquet, Nature 537 (2016) 210.
[3] B. Corry, J. Phys. Chem. B 112 (2008) 1427.
[4] B. Corry, MRS Bull. 42 (2017) 306.
[5] L. Bocquet, Nat. Mater. 19 (2020) 254.
[6] A. Sam, R. Hartkamp, S.K. Kannam, J.S. Babu, S.P. Sathian, P.J. Daivis, B.D. Todd, Mol. Simul. (2020) 1.
[7] C. Song, B. Corry, J. Phys. Chem. B 113 (2009) 7642.
[8] M. Thomas, B. Corry, Philosophical Transactions of the Royal Society A: Mathematical, Phys. Eng. Sci. 374 (2016) 20150020.
[9] S. Joseph, R.J. Mashl, E. Jakobsson, N.R. Aluru, Nano Lett. 3 (2003) 1399.
[10] Q. Li, D. Yang, J. Shi, X. Xu, S. Yan, Q. Liu, Desalination 379 (2016) 164.
[11] B. Corry, Energy Environ. Sci. 4 (2011) 751.
[12] A. Ghoufi, A. Szymczyk, P. Malfreyt, Sci. Rep. 6 (2016) 28518.
[13] A. Sam, V.P. Kurupath, S.P. Sathian, Phys. Chem. Chem. Phys. 21 (2019) 6566.
[14] J.H. Walther, K. Ritos, E.R. Cruz-Chu, C.M. Megaridis, P. Koumoutsakos, Nano Lett 13 (2013) 1910.
[15] K. Takata, Prog. Histochem. Cytochem. 39 (2004) 1.
[16] H. Sui, B.-G. Han, J.K. Lee, P. Walian, B.K. Jap, Nature 414 (2001) 872.
[17] J.S. Hub, B.L. De Groot, Proc. Natl. Acad. Sci. 105 (2008) 1198.
[18] D.F. Savage, J.D. O'Connell, L.J. Miercke, J. Finer-Moore, R.M. Stroud, Proc. Natl. Acad. Sci. 107 (2010) 17164.
[19] C. Tang, Y. Zhao, R. Wang, C. Hélix-Nielsen, A. Fane, Desalination 308 (2013) 34.
[20] Y. Li, S. Qi, M. Tian, W. Widjajanti, R. Wang, Desalination 467 (2019) 103.
[21] A. Giwa, S. Hasan, A. Yousuf, S. Chakraborty, D. Johnson, N. Hilal, Desalination 420 (2017) 403.
[22] S. Gravelle, L. Joly, F. Detcheverry, C. Ybert, C. Cottin-Bizonne, L. Bocquet, Proc. Natl. Acad. Sci. 110 (2013) 16367.
[23] S. Gravelle, L. Joly, C. Ybert, L. Bocquet, J. Chem. Phys. 141 (2014) 18C526.
[24] C. Han, D. Tang, D. Kim, Colloids Surf. A: Physicochem. Eng. Asp. 481 (2015) 38.
[25] M. Shahbabaei, D. Kim, Phys. Chem. Chem. Phys. 22 (2020) 1333.
[26] D. Tang, D. Kim, Appl. Therm. Eng. 72 (2014) 120.
[27] M. Shahbabaei, D. Kim, Phys. Chem. Chem. Phys. 19 (2017) 20749.
[28] M. Razmkhah, A. Ahmadpour, M.T.H. Mosavian, F. Moosavi, Desalination 407 (2017) 103.
[29] W. Li, W. Wang, X. Zheng, Z. Dong, Y. Yan, J. Zhang, Comput. Mater. Sci. 136 (2017) 60.
[30] W. Li, W. Wang, Y. Zhang, Y. Yan, P. Král, J. Zhang, Carbon 129 (2018) 374.
[31] X. Zhang, W. Zhou, F. Xu, M. Wei, Y. Wang, Nanoscale 10 (2018) 13242.
[32] A. Nalaparaju, J. Wang, J. Jiang, Advanced Theory and Simulations 3 (2020) 2000025.
[33] H. Hadidi, R. Kamali, Comput. Mater. Sci. 185 (2020) 109978.
[34] B. Balannec, A. Ghoufi, A. Szymczyk, J. Membr. Sci. 552 (2018) 336.
[35] R. Garcia-Fandino, M.S.P. Sansom, Proc. Natl. Acad. Sci. 109 (2012) 6939.
[36] G. Zuo, R. Shen, S. Ma, W. Guo, ACS Nano 4 (2009) 205.
[37] C.K. Tan, K.P. Loh, J.T. Thong, C.H. Sow, H. Zhang, Diam. Relat. Mater. 14 (2005) 902.
[38] Z. Tsakadze, I. Levchenko, K. Ostrikov, S. Xu, Carbon 45 (2007) 2022.
[39] W. Wang, Y. Lin, C. Kuo, Diam. Relat. Mater. 14 (2005) 907.
[40] I.-C. Chen, L.-H. Chen, X.-R. Ye, C. Daraio, S. Jin, C.A. Orme, A. Quist, R. Lal, Appl. Phys. Lett. 88 (2006) 153102.
[41] C.M. Yeh, M.Y. Chen, J. Hwang, J.-Y. Gan, C.S. Kou, Nanotechnology 17 (2006) 5930.
[42] J.-C. Charlier, G.-M. Rignanese, Phys. Rev. Lett. 86 (2001) 5970.
[43] H.J.C. Berendsen, J.R. Grigera, T.P. Straatsma, J. Phys. Chem. 91 (1987) 6269.
[44] C. Vega, J.L.F. Abascal, Phys. Chem. Chem. Phys. 13 (2011) 19663.
[45] A.T. Celebi, C.T. Nguyen, R. Hartkamp, A. Beskok, J. Chem. Phys. 151 (2019) 174705.
[46] D. Cohen-Tanugi, J.C. Grossman, Nano Lett. 12 (2012) 3602.
[47] R.W. Hockney, J.W. Eastwood, Computer Simulation Using Particles, CRC Press, 1988.
[48] J.-P. Ryckaert, G. Ciccotti, H.J. Berendsen, J. Comput. Phys. 23 (1977) 327.
[49] S. Plimpton, J. Comput. Phys. 117 (1995) 1.
[50] G. Cicero, J.C. Grossman, E. Schwegler, F. Gygi, G. Galli, J. Am. Chem. Soc. 130 (2008) 1871.
[51] J. Azamat, J.J. Sardroodi, A. Rastkar, RSC Adv. 4 (2014) 63712.
[52] V.P. Kurupath, S.K. Kannam, R. Hartkamp, S.P. Sathian, Phys. Chem. Chem. Phys. 20 (2018) 16005.
[53] L. Liu, G.N. Patey, J. Chem. Phys. 141 (2014) 18C518.
[54] U. Zimmerli, P.G. Gonnet, J.H. Walther, P. Koumoutsakos, Nano Lett. 5 (2005) 1017.
[55] J.A. Thomas, A.J.H. McGaughey, J. Chem. Phys. 128 (2008), 084715.
[56] A. Kalra, S. Garde, G. Hummer, Proc. Nat. Acad. Sci. 100 (2003) 10175.
[57] P.-A. Cazade, R. Hartkamp, B. Coasne, J. Phys. Chem. C 118 (2014) 5061.
[58] J.H. Walther, R. Jaffe, T. Halicioglu, P. Koumoutsakos, J. Phys. Chem. B 105 (2001) 9980.
[59] J.L. Rivera, C. McCabe, P.T. Cummings, Nano Lett. 2 (2002) 1427.
[60] A. Sam, S.K. Kannam, R. Hartkamp, S.P. Sathian, J. Chem. Phys. 146 (2017) 234701.
[61] M.K. Borg, D.A. Lockerby, K. Ritos, J.M. Reese, J. Membr. Sci. 567 (2018) 115.
[62] R. Hartkamp, B. Coasne, J. Chem. Phys. 141 (2014) 124508.
[63] J.S. Babu, S.P. Sathian, J. Chem. Phys. 134 (2011) 194509.